LETTER

Human contribution to more–intense precipitation extremes

Seung-Ki Min[1], Xuebin Zhang[1], Francis W. Zwiers[1]† & Gabriele C. Hegerl[2]

Extremes of weather and climate can have devastating effects on human society and the environment[1,2]. Understanding past changes in the characteristics of such events, including recent increases in the intensity of heavy precipitation events over a large part of the Northern Hemisphere land area[3–5], is critical for reliable projections of future changes. Given that atmospheric water-holding capacity is expected to increase roughly exponentially with temperature—and that atmospheric water content is increasing in accord with this theoretical expectation[6–11]—it has been suggested that human-influenced global warming may be partly responsible for increases in heavy precipitation[3,5,7]. Because of the limited availability of daily observations, however, most previous studies have examined only the potential detectability of changes in extreme precipitation through model–model comparisons[12–15]. Here we show that human-induced increases in greenhouse gases have contributed to the observed intensification of heavy precipitation events found over approximately two-thirds of data-covered parts of Northern Hemisphere land areas. These results are based on a comparison of observed and multi-model simulated changes in extreme precipitation over the latter half of the twentieth century analysed with an optimal fingerprinting technique. Changes in extreme precipitation projected by models, and thus the impacts of future changes in extreme precipitation, may be underestimated because models seem to underestimate the observed increase in heavy precipitation with warming[16].

We compare observed and simulated changes in extreme precipitation based on the annual maxima of daily (RX1D) and five-day consecutive (RX5D) precipitation amounts for the second half of the twentieth century. We chose these indices because they characterize extreme events that often cause impacts on society[1,2], and because these annual extremes can be used to estimate the probability of rare events such as 100-year return values, which are used in the design of infrastructure. We use the Hadley Centre global land-based gridded climate extremes data set (HadEX)[4], which is based on daily observations from 6,000 stations and covers the period 1951–2003. We restrict our analysis to the period 1951–99 for comparison with model simulations and because of loss of coverage at the end of the period of record (Supplementary Information). Multi-model simulations were obtained from the Coupled Model Intercomparison Project Phase 3 (CMIP3) archive and from individual modelling centres (Supplementary Table 1). The RX1D and RX5D indices were calculated from all available simulations from eight models. We used the 1951–99 segments of simulations of the twentieth century with either historical anthropogenic forcing (greenhouse gases and other anthropogenic factors including aerosols, ANT; 6 models, 19 runs) or a combination of historical natural (solar and volcanic) plus anthropogenic forcing (ALL; 5 models, 16 runs). Three models provided both ANT and ALL runs. We also used unforced control simulations (CTL; 106 non-overlapping 49-year segments).

Owing to the high spatial variability of precipitation and the sparseness of the observing network in many regions, estimates of area means

of extreme precipitation may be uncertain; for example, for regions where the distribution of individual stations does not adequately sample the spatial variability of extreme values across the region. In order to reduce the effects of this source of uncertainty on area means, and to improve representativeness and inter-comparability, we standardized values at each grid-point before estimating large area averages by mapping extreme precipitation amounts onto a zero-to-one scale[15]. The resulting 'probability-based index' (PI) equalizes the weighting given to grid-points in different locations and climatic regions in large area averages and facilitates comparison between observations and model simulations[15,17,18]. Observed and simulated annual extremes are converted to PI by fitting a separate generalized extreme value (GEV) distribution[15,19] to each 49-year time series of annual extremes and replacing values with their corresponding percentiles on the fitted distribution. Model PI values are interpolated onto the HadEX grid to facilitate comparison with observations (see Methods Summary and Supplementary Information for details).

Figure 1 shows the spatial patterns of the observed and multi-model mean trends in PI for RX1D and RX5D during 1951–99. Trends are shown only for grid-points with more than 40 years of observations. This confines the analysis to Northern Hemisphere land areas, including North America and Eurasia (including India). Spatial coverage for RX5D is somewhat greater than for RX1D due to broader spatial interpolation of the available station values[4], possibly affecting reliability (Supplementary Information). We therefore also analyse RX5D only at locations where RX1D is available, and find that our main detection results are not affected (Supplementary Fig. 1). Observations show overall increasing trends in PI, with 65% and 61% of the total data-covered areas having positive trends for RX1D and RX5D, respectively. The multi-model mean from ANT simulations shows positive trends in both extreme indices almost everywhere, consistent with future projections[17–20], but with smaller amplitude than observed. Multi-model ALL simulations exhibit similar moderate increasing trends in RX1D, but show a mixed pattern of moistening and drying for RX5D (see below).

In order to consider long-term changes in extreme precipitation, we calculate non-overlapping five-year mean PI anomaly time series for 1955–99 and append a four-year mean for 1951–54. The time evolution of five-year mean PI anomalies averaged over Northern Hemisphere land (using the locations plotted in Fig. 1) is shown in Fig. 2. Observations exhibit increasing trends for both RX1D and RX5D, in accord with previous studies[3–5]. The ANT simulations show also increasing trends, but with smaller amplitudes than observed, consistent with Fig. 1. No individual simulation has a trend as strong as observed (Supplementary Fig. 2). The ALL simulations exhibit weak positive trends globally in RX1D, and spatially variable weak positive and negative trends in both RX1D and RX5D. This seems to be partly due to the inclusion of natural forcing (NAT) in the ALL simulations, which on its own would have induced long-term overall cooling and drying trends for the analysis period[13,15], thus reducing the positive trends in intense precipitation due to ANT forcing (Supplementary Fig. 3). Considering that models underestimate the observed changes

---

[1]Climate Research Division, Environment Canada, Toronto, Ontario M3H5T4, Canada. [2]School of GeoSciences, University of Edinburgh, Edinburgh EH9 3JW, UK. †Present address: Pacific Climate Impacts Consortium, University of Victoria, Victoria, British Columbia V8W2Y2, Canada.
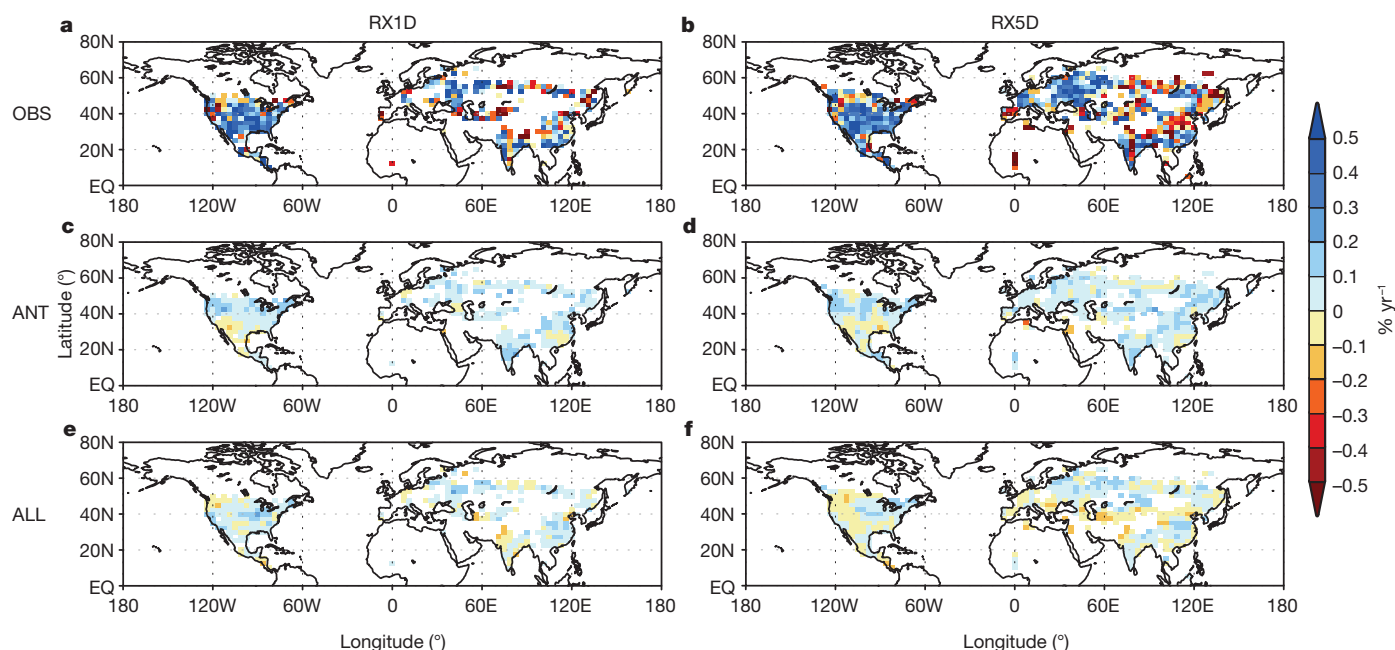
Figure 1 | Geographical distribution of trends of extreme precipitation indices (PI) during 1951–99. a, b, Observations (OBS); **c, d,** model simulations with anthropogenic (ANT) forcing; **e, f,** model simulations with anthropogenic plus natural (ALL) forcing. For each pair of panels, results are shown for annual maximum daily (RX1D) and five-day (RX5D) precipitation amounts. For models, ensemble means of trends from individual simulations are displayed. Units: per cent probability per year.

in precipitation extremes[16], and that smaller trends are more likely to be masked by noise, the ANT signal should be more detectable than the ALL signal in observations (see Supplementary Information for more discussion).

We use a rigorous optimal detection method[21] to compare observed and simulated long-term variations in PI (see Methods Summary for details). In this method, observed patterns are regressed onto multi-model

simulated responses to external forcing (fingerprint patterns). The resulting best estimates and uncertainty ranges of the regression coefficients (or scaling factors) are analysed to determine whether the fingerprints are present in the observations. For detection, the estimated scaling factors should be positive and uncertainty ranges should exclude zero. If the uncertainty ranges also include unity, the model patterns are considered to be consistent with observations. Model performance in
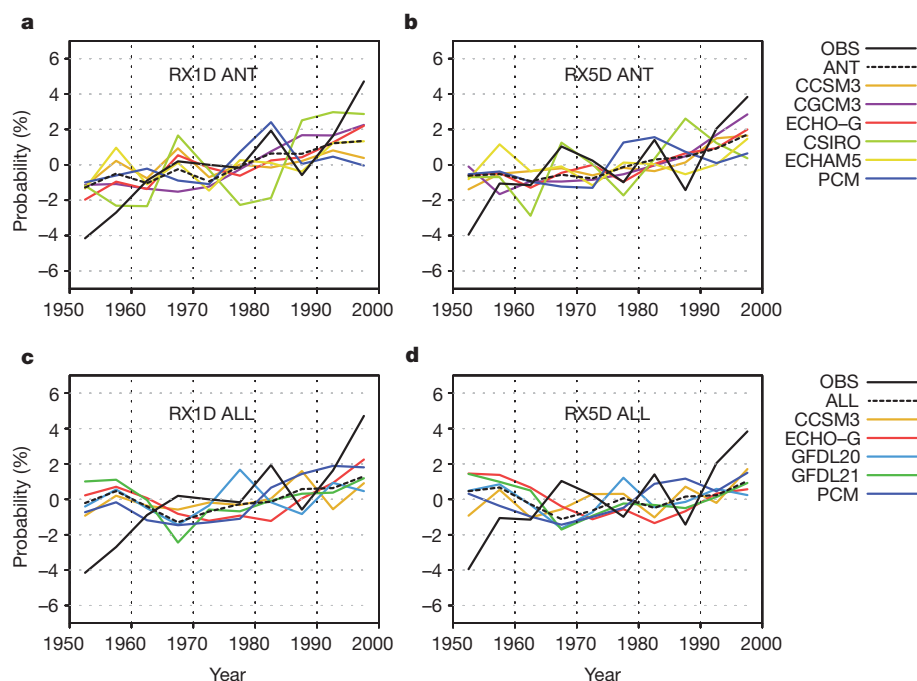

Figure 2 | Time series of five-year mean area-averaged PI anomalies over Northern Hemisphere land during 1951–99. a, b, Model simulations with anthropogenic (ANT) forcing; **c, d,** model simulations with anthropogenic plus natural (ALL) forcing. For each pair of panels, results are shown for RX1D and RX5D precipitation amounts. Black solid lines are observations and dashed lines represent multi-model means. Coloured lines indicate results for individual model averages (see Supplementary Table 1 for the list of climate model simulations and Supplementary Fig. 2 for time series of individual simulations). Each time series is represented as anomalies with respect to its 1951–99 mean.

simulating internal variability must be considered carefully[13,22] to avoid spurious detection. A standard residual consistency test[22] is employed for this purpose and our detection analysis is confined to a reduced space in which the models used here simulate internal variability reasonably well (see Supplementary Information for more details).

The time evolution of five-year mean regionally averaged PI values was analysed using the optimal detection technique for both RX1D and RX5D. Given the limited data availability, we choose regions that would span either the meridional variation of changes in extremes (that is, the northern mid-latitudes and tropics), or the zonal variation in extremes (that is, Eurasia and the Americas), and repeated our detection analysis for both subdivisions. Figure 3 shows the results of four optimal detection analyses using the time evolution of extreme precipitation indices averaged over the Northern Hemisphere, over northern mid-latitudes and northern tropics individually, and over these two regions simultaneously for 1951–99. Regression coefficients obtained when using ANT fingerprints are significantly greater than zero for both RX1D and RX5D, indicating that anthropogenic influence is detectable in the observed temporal or spatiotemporal changes in extreme precipitation for this period. Results from a space-time analysis using the zonal decomposition also support our findings (Supplementary Fig. 4). The signals are detected only when PI is averaged

over hemispheric and continental scales, consistent with previous detectability studies[15]; detection fails when smaller sub-continental areas are considered (not shown). The ALL signal is detected in RX1D albeit less robustly, which reflects the lower signal-to-noise ratio due to the inclusion of NAT forcing (see also Supplementary Information).

Best estimates of the regression coefficients are larger than unity (Fig. 3), indicating that the extreme precipitation response to ANT forcing may be underestimated by models compared to observed changes, consistent with previous suggestions based on satellite observations over the tropical oceans[16] and observed changes in annual precipitation amounts over the global and Arctic land areas[23,24]. The residual consistency test[22] as well as simple comparison of variances (Supplementary Table 2) show that the models simulate the internal variability of low-frequency hemispheric land mean PI reasonably well (Supplementary Information). Nevertheless, ANT detection generally continues to hold when our estimate of internal variability is doubled (dashed lines in Fig. 3).

Figure 3 also shows that ANT can be more robustly detected in RX1D than RX5D. The signal amplitude, as measured by the slope of the linear trend, is larger in model simulated RX1D (Supplementary Information). Observed trends are also larger in RX1D than in RX5D. This is consistent with previous findings[6,9,16] that changes in more extreme precipitation follow the Clausius–Clapeyron relationship (which describes the rate of increase of atmospheric moisture with warming) more closely. Atmospheric circulation changes from global warming can also influence the pattern of extreme precipitation[25] but this is unlikely to substantially affect our findings because the Northern Hemisphere mid-latitude land region analysed here seems to be influenced predominantly by the Clausius–Clapeyron relationship[9,25–27] (see Supplementary Information for more discussion concerning physical mechanisms). A series of sensitivity tests show that our detection results are robust to observational data coverage change, interpolation methods, influence of natural climate variability on observations, and different model sampling (see Supplementary Information).

Our results provide to our knowledge the first formal identification of a human contribution to the observed intensification of extreme precipitation. We used probability-based indices of precipitation extremes that facilitate the comparison of observations with models[15,28]. Our results also show that the global climate models we used may have underestimated the observed trend, which implies that extreme precipitation events may strengthen more quickly in the future than projected and that they may have more severe impacts than estimated. There are, however, uncertainties related to observational limitations[3,5], missing or uncertain external forcings[13,29] and model performance[14,26–29].

METHODS SUMMARY

Probability-based index. We use the GEV distribution[19] to convert 49-year time series of the largest one-day and five-day precipitation accumulations annually, RX1D and RX5D, into corresponding time series of PI at each grid-point. A GEV distributed variable x has a cumulative distribution function that is characterized by location (μ), scale (σ) and shape (ξ) parameters as follows:

$$F(x; \mu, \sigma, \xi) = \begin{cases} \exp\left[-\exp\left\{-\dfrac{x-\mu}{\sigma}\right\}\right], & \xi = 0 \\ \exp\left[-\left\{1 + \xi \dfrac{x-\mu}{\sigma}\right\}^{-\xi^{-1}}\right], & \xi \neq 0, \quad 1 + \xi \dfrac{x-\mu}{\sigma} > 0. \end{cases} \quad (1)$$

The parameters for a given grid-point are estimated by fitting the GEV distribution to individual 49-year (or shorter) time series of observed or model-simulated annual precipitation maxima by the method of maximum likelihood[30]. We do not vary GEV parameters with time. Each annual maximum for a given grid-point and data set is converted to PI by evaluating the corresponding fitted cumulative distribution function at the value of that annual maximum. Stronger annual precipitation extremes will yield PI values closer to 1, while weaker extremes will yield PI values closer to 0. See the Supplementary Information for more details.

Detection and attribution. We use an optimal regression method[21] in which observations (**y**) are expressed as a sum of scaled model-simulated fingerprint patterns (**X**) plus internal climate variability (ε) as $\mathbf{y} = \mathbf{X}\boldsymbol{\beta} + \boldsymbol{\varepsilon}$. The scaling factors

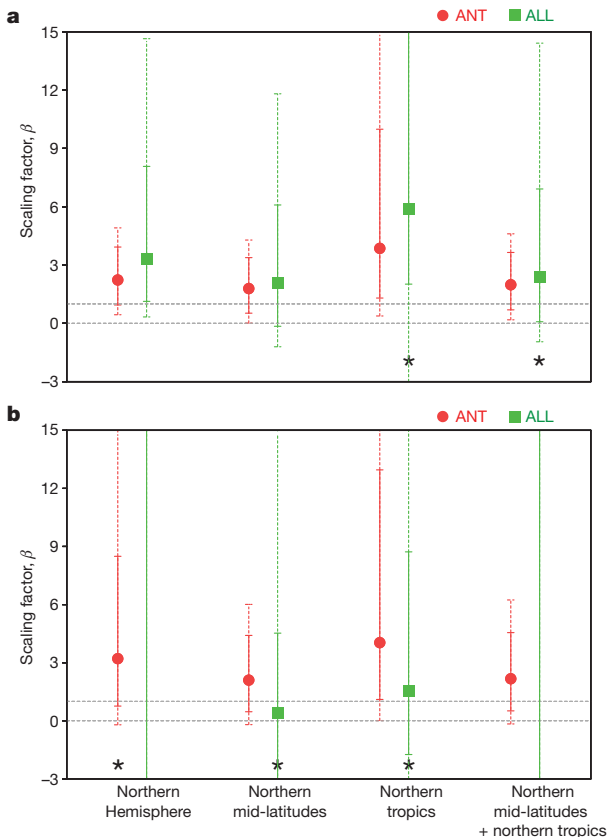**Figure 3 | Results from optimal detection analyses of extreme precipitation indices. a**, PI for RX1D, **b**, PI for RX5D, both over the period 1951–99. Best estimates (data points) and 5–95% uncertainty ranges (error bars) of regression coefficients β are displayed for one-signal fingerprint detection analyses for ANT (red) and ALL (green), when using five-year mean PI averaged over the Northern Hemisphere, the northern mid-latitudes (30° N–65° N), the northern tropics (0°–30° N) (10-dimensional time vector in all three cases), and when using two regional averages combined (northern mid-latitudes + northern tropics; 20-dimensional space-time vector). Dashed error bars show β ranges when the internal variability is doubled. An error bar without a data point represents unbounded uncertainty in estimating β ranges. The two grey dashed horizontal lines represent zero and unity. An asterisk indicates passage of the residual consistency test[22] only when the internal variability is doubled, suggesting insufficient model variability (see text for more details).

β adjust the magnitude of the fingerprints to best match the observations. Fingerprints are estimated from the means of forced (ANT or ALL) simulations and internal variability is estimated from CTL simulations (see Supplementary Information). The regression is fitted using the total least squares method[21]. Detection analyses are conducted in a reduced space in which observations and simulated patterns of change are represented by their projections onto the leading empirical orthogonal functions (EOFs) of internal variability. In the 1951–99 analysis (Fig. 3), the four leading EOFs are retained, which explain about 52–63% of the total variance.

1. Parry, M. L. Canziani, O. F., Palutikof, J. P., van der Linden, P. J. & Hanson, C. E. (eds) *Climate Change 2007: Impacts, Adaptation and Vulnerability* (Cambridge Univ. Press, 2007).
2. Peterson, T. C. *et al.* in *Weather and Climate Extremes in a Changing Climate. Regions of Focus: North America, Hawaii, Caribbean, and U.S. Pacific Islands* (eds Karl, T. R. *et al.*) 11–34 (Synthesis and Assessment Product 3.3, US Climate Change Science Program, Washington DC, 2008).
3. Groisman, P. & Ya. *et al.* Trends in intense precipitation in the climate record. *J. Clim.* **18,** 1326–1350 (2005).
4. Alexander, L. V. *et al.* Global observed changes in daily climatic extremes of temperature and precipitation. *J. Geophys. Res.* **111,** D05109, doi:10.1029/2005JD006290 (2006).
5. Trenberth, K. E. *et al.* in *Climate Change 2007: The Physical Science Basis* (eds Solomon, S. *et al.*) 235–336 (Cambridge Univ. Press, 2007).
6. Allen, M. R. & Ingram, W. J. Constraints on future changes in climate and the hydrologic cycle. *Nature* **419,** 224–232 (2002).
7. Trenberth, K. E., Dai, A., Rasmussen, R. M. & Parsons, D. B. The changing character of precipitation. *Bull. Am. Meteorol. Soc.* **84,** 1205–1217 (2003).
8. Wentz, F. J. & Schabel, M. Precise climate monitoring using complementary satellite data sets. *Nature* **403,** 414–416 (2000).
9. Pall, P., Allen, M. R. & Stone, D. A. Testing the Clausius-Clapeyron constraint on changes in extreme precipitation under CO_2 warming. *Clim. Dyn.* **28,** 351–363 (2007).
10. Santer, B. D. *et al.* Identification of human-induced changes in atmospheric moisture content. *Proc. Natl Acad. Sci. USA* **104,** 15248–15253 (2007).
11. Willett, K. M., Gillett, N. P., Jones, P. D. & Thorne, P. W. Attribution of observed surface humidity changes to human influence. *Nature* **449,** 710–712 (2007).
12. Hegerl, G. C., Zwiers, F. W., Stott, P. A. & Kharin, V. V. Detectability of anthropogenic changes in annual temperature and precipitation extremes. *J. Clim.* **17,** 3683–3700 (2004).
13. Hegerl, G. C. *et al.* in *Climate Change 2007: The Physical Science Basis* (eds Solomon, S. *et al.*) 663–745 (Cambridge Univ. Press, 2007).
14. Kiktev, D., Caesar, J., Alexander, L. V., Shiogama, H. & Collier, M. Comparison of observed and multimodeled trends in annual extremes of temperature and precipitation. *Geophys. Res. Lett.* **34,** L10702, doi:10.1029/2007GL029539 (2007).
15. Min, S.-K., Zhang, X. B., Zwiers, F. W., Friederichs, P. & Hense, A. Signal detectability in extreme precipitation changes assessed from twentieth century climate simulations. *Clim. Dyn.* **32,** 95–111 (2009).
16. Allan, R. P. & Soden, B. J. Atmospheric warming and the amplification of precipitation extremes. *Science* **321,** 1481–1484 (2008).
17. Tebaldi, C., Hayhoe, K., Arblaster, J. M. & Meehl, G. A. Going to the extremes: an intercomparison of model-simulated historical and future changes in extreme events. *Clim. Change* **79,** 185–211 (2006).
18. Kharin, V. V., Zwiers, F. W., Zhang, X. & Hegerl, G. C. Changes in temperature and precipitation extremes in the IPCC ensemble of global coupled model simulations. *J. Clim.* **20,** 1419–1444 (2007).
19. Zwiers, F. W. & Kharin, V. V. Changes in the extremes of the climate simulated by CCC GCM2 under CO_2 doubling. *J. Clim.* **11,** 2200–2222 (1998).
20. Meehl, G. *et al.* in *Climate Change 2007: The Physical Science Basis* (eds Solomon, S. *et al.*) 747–845 (Cambridge Univ. Press, 2007).
21. Allen, M. R. & Stott, P. A. Estimating signal amplitudes in optimal fingerprinting. Part I: theory. *Clim. Dyn.* **21,** 477–491 (2003).
22. Allen, M. R. & Tett, S. F. B. Checking for model consistency in optimal fingerprinting. *Clim. Dyn.* **15,** 419–434 (1999).
23. Zhang, X. *et al.* Detection of human influence on 20th century precipitation trends. *Nature* **448,** 461–465 (2007).
24. Min, S.-K., Zhang, X. & Zwiers, F. Human-induced Arctic moistening. *Science* **320,** 518–520 (2008).
25. Emori, S. & Brown, S. J. Dynamic and thermodynamic changes in mean and extreme precipitation under changed climate. *Geophys. Res. Lett.* **32,** L17706, doi:10.1029/2005GL023272 (2005).
26. O'Gorman, P. A. & Schneider, T. The physical basis for increases in precipitation extremes in simulations of 21st-century climate change. *Proc. Natl Acad. Sci. USA* **106,** 14773–14777 (2009).
27. Sugiyama, M., Shiogama, H. & Emori, S. Precipitation extreme changes exceeding moisture content increases in MIROC and IPCC climate models. *Proc. Natl Acad. Sci. USA* **107,** 571–575 (2010).
28. Durman, C. F., Gregory, J. M., Hassell, D. C., Jones, R. G. & Murphy, J. M. A comparison of extreme European daily precipitation simulated by a global and a regional climate model for present and future climates. *Q. J. R. Meteorol. Soc.* **127,** 1005–1015 (2001).
29. Randall, D. A. *et al.* in *Climate Change 2007: The Physical Science Basis* (eds Solomon, S. *et al.*) 589–662 (Cambridge Univ. Press, 2007).
30. Kharin, V. V. & Zwiers, F. W. Estimating extremes in transient climate change simulations. *J. Clim.* **18,** 1156–1173 (2005).

Author Contributions S.-K.M. carried out analysis. X.Z., F.W.Z. and G.C.H. contributed to the analysis. All authors discussed the results and contributed to writing the paper.

Author Information Reprints and permissions information is available at www.nature.com/reprints. The authors declare no competing financial interests. Readers are welcome to comment on the online version of this article at www.nature.com/nature. Correspondence and requests for materials should be addressed to S.-K.M. (seung-ki.min@ec.gc.ca) or F.W.Z (fwzwiers@uvic.ca).

CORRECTIONS & AMENDMENTS

Corrigendum: Human contribution to more-intense precipitation extremes

Seung-Ki Min, Xuebin Zhang, Francis W. Zwiers & Gabriele C. Hegerl

Supplementary Figs 8, 9 and 11 of this Article each inadvertently included results for an extraneous empirical orthogonal function (EOF)—two extraneous EOFs in the case of the right-hand column of Supplementary Fig. 8. The time mean was removed prior to the detection analysis, so the rank of the covariance matrix (which determines the maximum number of EOFs required to describe the data fully) should be nine for the time series of Northern Hemisphere mean five-year means for 1951–1999 and eight for 1955–1999. Similarly, when combining two domains such as the Northern mid-latitudes and tropics ("Nmid+Ntro"), the rank of the covariance matrix is 18 for 1951–1999. Results for ten EOFs shown in the left panel of Supplementary Fig. 8 and the lower-right panel of Supplementary Fig. 9 reflect numerical artefacts and were incorrectly included in these plots, as were results for 19 and 20 EOFs in the right panel of Supplementary Fig. 8, and for nine EOFs in Supplementary Fig. 11. In addition, for the 1951–1999 single-domain analyses the 1955–1999 means were removed from the second set of control simulations prior to the detection analysis rather than the 1951–1999 means. This small error affected detection results using ten EOFs only in Supplementary Fig. 8. The corrected Supplementary Figs 8, 9 and 11 are provided as Supplementary Information to this Corrigendum. Our conclusions and results are unaffected.

Supplementary Information is available in the online version of this Corrigendum.